Chemical Science

ROYAL SOCIETY OF CHEMISTRY

EDGE ARTICLE

View Article Online
View Journal

Check for updates

Cite this: DOI: 10.1039/d6sc00563b

All publication charges for this article have been paid for by the Royal Society of Chemistry

Design rules for ternary CO_2 hydrogenation catalysts *via* literature-sourced network construction and analysis

Yoshiki Hasukawa, [a] Fernando Garcia-Escobar, [a] Shun Nishimura, [b] Keisuke Takahashi *[ac] and Lauren Takahashi *[a]

The development of CO_2 hydrogenation catalysts has largely depended on researchers's trial and error efforts. However, exploring unreported ternary catalysts requires substantial time and cost, highlighting the need for more efficient screening strategies. This study adopts a data-driven informatics approach where literature data is restructured into networks to reveal systematic relationships between reaction conditions and CO_2 conversion. Knowledge extracted from the catalyst combination network further enables the identification of promising ternary catalysts. NiMnPr/Al_2O_3 and NiMnCe/Al_2O_3 for CO_2 hydrogenation are rapidly identified and experimentally validated, exhibiting higher CO_2 conversion than their corresponding binary catalysts. Moreover, detailed characterization is carried out for NiMnPr/Al_2O_3. These findings and analysis demonstrate that mapping multidimensional data into networks provides a powerful strategy for uncovering correlated variables and facilitating intuitive, highly efficient catalyst development and understanding.

Received 20th January 2026
Accepted 6th April 2026

DOI: 10.1039/d6sc00563b

rsc.li/chemical-science

Open Access Article. Published on 09 April 2026. Downloaded on 4/30/2026 7:20:59 AM.
This article is licensed under a Creative Commons Attribution-NonCommercial 3.0 Unported Licence.

1 Introduction

CO_2 hydrogenation, the conversion of carbon dioxide into methane, is a crucial reaction in contexts such as carbon neutrality and space technologies.[1–5] Catalysts centered on Ru and Ni have been explored to date.[6–12] Ru has demonstrated activity at low temperature but is expensive and scarce. Meanwhile, Ni is inexpensive but faces challenges of exhibiting higher reaction temperature and lower catalytic activity compared with Ru.[13–15] Since Ru-based catalysts are limited by high cost and scarcity, developing Ni-based catalysts with high performance at low temperature is a critical strategy for the practical application of CO_2 hydrogenation.[16,17] In particular, previous catalyst explorations have largely centered on binary catalysts *via* trial-and-error approaches, whereas ternary catalysts remain unexplored.[18] Given that specific combinations of elements can generate synergistic interactions, in which the catalytic activity deviates from that of the individual components or their simple average, ternary systems hold strong potential.[19] Therefore, ternary catalysts are explored as they may realize synergistic performance gains unattainable with binary formulations.

Trial-and-error catalyst development is often inefficient in terms of both cost and time.[20] In contrast, data-driven catalyst informatics can extract hidden trends and patterns from diverse variables in catalysts data, thereby offering opportunities for more efficient and useful catalyst discovery.[21–24] Machine learning has been used to successfully discover previously unreported and potentially promising catalysts.[25,26] However, a major challenge lies in the black-box nature of machine learning, which obscures both the reasoning behind the predictions and the underlying learning process in the dataset.[27] To address this problem, catalyst network analysis utilizing graph theory has emerged. This approach visualizes the relationship between catalytic activity and multidimensional variables, providing human-readable insights.[28–30] Based on the positional relationships within the network, it enables reaction condition optimization, efficient catalyst screening, and catalyst design.

Based on the above context and challenges, multidimensional analysis and ternary catalysts design through catalyst screening are performed for CO_2 hydrogenation dataset. Network construction and analysis are used in order to better understand the relationship between multidimensional factors and CO_2 conversion and to improve the efficiency of ternary catalyst design from binary catalysts data, thereby providing a means for accelerated catalysts exploration.

[a]*Department of Chemistry, Hokkaido University, North 10, West 8, Sapporo 060-0810, Japan. E-mail: keisuke.takahashi@sci.hokudai.ac.jp; lauren.takahashi@sci.hokudai.ac.jp*

[b]*Graduate School of Advanced Science and Technology, Japan Advanced Institute of Science and Technology, 1–1 Asahidai, Nomi, Ishikawa 923-1292, Japan*

[c]*List Sustainable Digital Transformation Catalyst Collaboration Research Platform, Institute for Chemical Reaction Design and Discovery, Hokkaido University, Sapporo 001-0021, Japan*

© 2026 The Author(s). Published by the Royal Society of Chemistry

Open Access Article. Published on 09 April 2026. Downloaded on 4/30/2026 7:20:59 AM. This article is licensed under a Creative Commons Attribution-NonCommercial 3.0 Unported Licence.

2 Method

2.1 Data details

A dataset comprising 4051 entries collected from 100 papers is used for the network analysis of catalytic studies.[26] Table 1 summarizes the category of the dataset and their features. After removing entries containing missing values, 3531 entries are employed for network construction.

2.2 Preprocessing for network construction

To construct the network, the following features are utilized and preprocessed: base, base wt%, base 2, base 2 wt%, support, support wt%, calcination temperature (°C), calcination time (h), temperature (°C), W/F (mg_{Cat} mL min^{-1}), inert% in feed, and CO_2 conversion%. To better understand the relationship between catalyst information and catalyst activity, base wt%, base 2 wt%, support wt%, and CO_2 conversion% are clustered using the one dimensional *K*-means algorithm. The number of clusters for each dataset is decided based on the distribution of each variables. By this algorithm, base wt% is clustered into 5 bins (0.0–7.0%, 7.5–15.0%, 17.0–26.0%, 27.5–40.0%, 47.0–100.0%), base 2 wt% into 4 bins (0.0–3.0%, 4.0–10.0%, 12.5–17.0%, 25.0–37.5%), support wt% into 4 bins (0.0–60.7%, 62.5–80.0%, 81.0–91.5%, 92.0–100.0%), and CO_2 conversion into 10 bins (0.0–5.61%, 5.63–14.15%, 14.19–24.52%, 24.62–35.37%, 35.4–46.03%, 46.08–56.88%, 57.0–67.53%, 67.59–77.5%, 77.52–88.38%, 88.41–100.0%).

Two networks, N-1 and N-2, are constructed in this work. For N-1 network, each catalyst element is represented as a node along with its respective content. Here, nodes are defined as vertices which represents base, base 2, support, calcination temperature, calcination time, temperature, W/F, inert gas, CO_2 conversion. Edges are links that are added between CO_2 conversion and each of the other variables (base, base 2, support, calcination temperature (°C), calcination time (h), temperature (°C), W/F, inert% in feed) when the corresponding pair is observed together within the same record in the dataset. Note that this is purely a visualization outcome of the layout algorithm, and the geometric distances should not be interpreted as precise numerical distances since nodes sharing more edges are placed closer to each other. The layouts of both networks are constructed as undirected graphs *via* ForceAtlas2 algorithm within Gephi application to visualize the relationship of between CO_2 conversion and other features.[31,32] The edge weight is set to 1 for both networks. Node size is determined by degree ranking within a range of 10 to 40. Additionally, for visibility purposes, the labels are represented in a simplified manner on the network: base as b, base 2 as b2, support as s, calcination temperature as cTemp, calcination time as cTime, temperature as T, W/F as W/F, inert in feed as inert, and CO_2 conversion as conv. For example, one data (base: Ni, base wt%: 10.0, base 2: none, base 2 wt%: 0.0, support: Al_2O_3, support: wt%: 90.0, calcination temperature (°C): 600, calcination time (h): 4.0, temperature (°C): 350, W/F: 5.26, inert in feed%: 21.0, CO_2 conversion%: 25.552) of the network N-1 is represented as nodes: b-Ni: 7.5–15.0, b2-None, s-Al_2O_3: 81.0–91.5, cTemp: 600, cTime: 4.0, temp: 350, W/F: 5.26, inert: 21.0, and conv: 24.62–35.37 as shown in Fig. S1. In the network N-2, nodes are constructed by combining base and base 2 to represent the catalyst combinations. For example, one data (base: Ni, base wt%: 10.0, base 2: none, base 2 wt%: 0.0, support: Al_2O_3, support: wt%: 90.0, calcination temperature (°C): 600, calcination time (h): 4.0, temperature (°C): 350, W/F: 5.26, inert in feed%: 21.0, CO_2 conversion%: 25.552) is represented as nodes: Ni(7.5–15.0)None(), s-Al_2O_3: 81.0–91.5, cTemp: 600, cTime: 4.0, T: 350, W/F: 5.26, inert: 21.0, and conv: 24.62–35.37 as shown in Fig. S2.

Table 1 The features and their explanations in the dataset[26]

Category	Features
Catalyst information	Base
	Base wt%
	Base 2
	Base 2 wt%
	Support
	Support wt%
	Support 2
Preparation condition	Catalyst preparation method
	Calcination temperature (°C)
	Calcination time (h)
	Reduction temperature (°C)
	Reduction pressure (bar)
	Reduction time (h)
	Reduction H_2%
Reaction condition	Temperature (°C)
	Pressure (bar)
	W/F (mg_{Cat} mL min^{-1})
	Time on stream (h)
	CO% in feed
	Inert% in feed
	CH_4% in feed
	H_2O% in feed
	H_2/CO_2% in feed
Catalyst activity	CO_2 conversion%

2.3 Experimental

2.3.1 Catalyst preparation. The tested catalysts are prepared by impregnating a support oxide with water-soluble metallic precursors in combinations presented on Table 2.

Table 2 M1–M2–M3 combinations of the prepared γ-Al_2O_3-supported catalysts

Label	M1	M2	M3
NiMnCe/Al_2O_3	Ce	Ni	Mn
NiMnPr/Al_2O_3	Pr	Ni	Mn
NiMnBa/Al_2O_3	Ba	Mn	Ni
NiMnCo/Al_2O_3	Mn	Co	Ni
NiMnNa/Al_2O_3	Na	Ni	Mn
NiMnFe/Al_2O_3	Mn	Fe	Ni
NiMn/Al_2O_3	Mn	Ni	—
NiCe/Al_2O_3	Ce	Ni	—
NiPr/Al_2O_3	Pr	Ni	—
MnPr/Al_2O_3	Pr	Mn	—
Ni/Al_2O_3	Ni	—	—
Mn/Al_2O_3	Mn	—	—
Pr/Al_2O_3	Pr	—	—

© 2026 The Author(s). Published by the Royal Society of Chemistry

Open Access Article. Published on 09 April 2026. Downloaded on 4/30/2026 7:20:59 AM. This article is licensed under a Creative Commons Attribution-NonCommercial 3.0 Unported Licence.

γ-Alumina (γ-Al_2O_3, Kojundo Chemical Laboratory Co., Ltd, 99.0%) is used as support for catalysts. Iron(III) nitrate nonahydrate ($Fe(NO_3)_3 \cdot 9H_2O$, min. 99.0%) from Junsei Chemical Co., Ltd and nickel(II) nitrate hexahydrate ($Ni(NO_3)_2 \cdot 6H_2O$, Wako Special Grade), manganese(II) acetate tetrahydrate ($(CH_3COO)_2$-Mn, Wako Special Grade), cerium(III) nitrate hexahydrate ($Ce(NO_3)_3 \cdot 6H_2O$, Wako Special Grade), praseodymium(III) nitrate *n*-hydrate ($Pr(NO_3)_3 \cdot nH_2O$, 99.5%), barium acetate ($Ba(CH_3COO)_2$, min. 99.0%), cobalt(II) acetate ($(CH_3COO)_2Co \cdot 4H_2O$, Wako Special Grade), and sodium nitrate ($NaNO_3$, min. 99.0%) from FUJIFILM Wako Pure Chemical Corporation are used as precursors for the impregnated metals in the catalysts.

All catalysts are synthesized according to the following procedure. 2 g of the support (γ-Al_2O_3) are dispersed in 100 mL of pure water under continuous stirring. Separately, the metallic precursors for M1, M2 and M3 are each dissolved in 50 mL of pure water to achieve 5 wt% each in the final catalyst based on the calculated precursor quantities for complete impregnation. The metallic solutions are sequentially added to the support dispersion at 5 minutes intervals in M1–M2–M3 order. After stirring for 1 hour, the dispersion is aged 24 hours without stirring at room temperature. The stirring is restarted and the water is evaporated. The remaining powder is collected and dried at 80 °C for 12 hours. Finally, the material is ground in a mortar, calcined at 500 °C for 3.0 hours and ground again before testing. For comparison, unary and binary catalysts are also prepared by the same procedure.

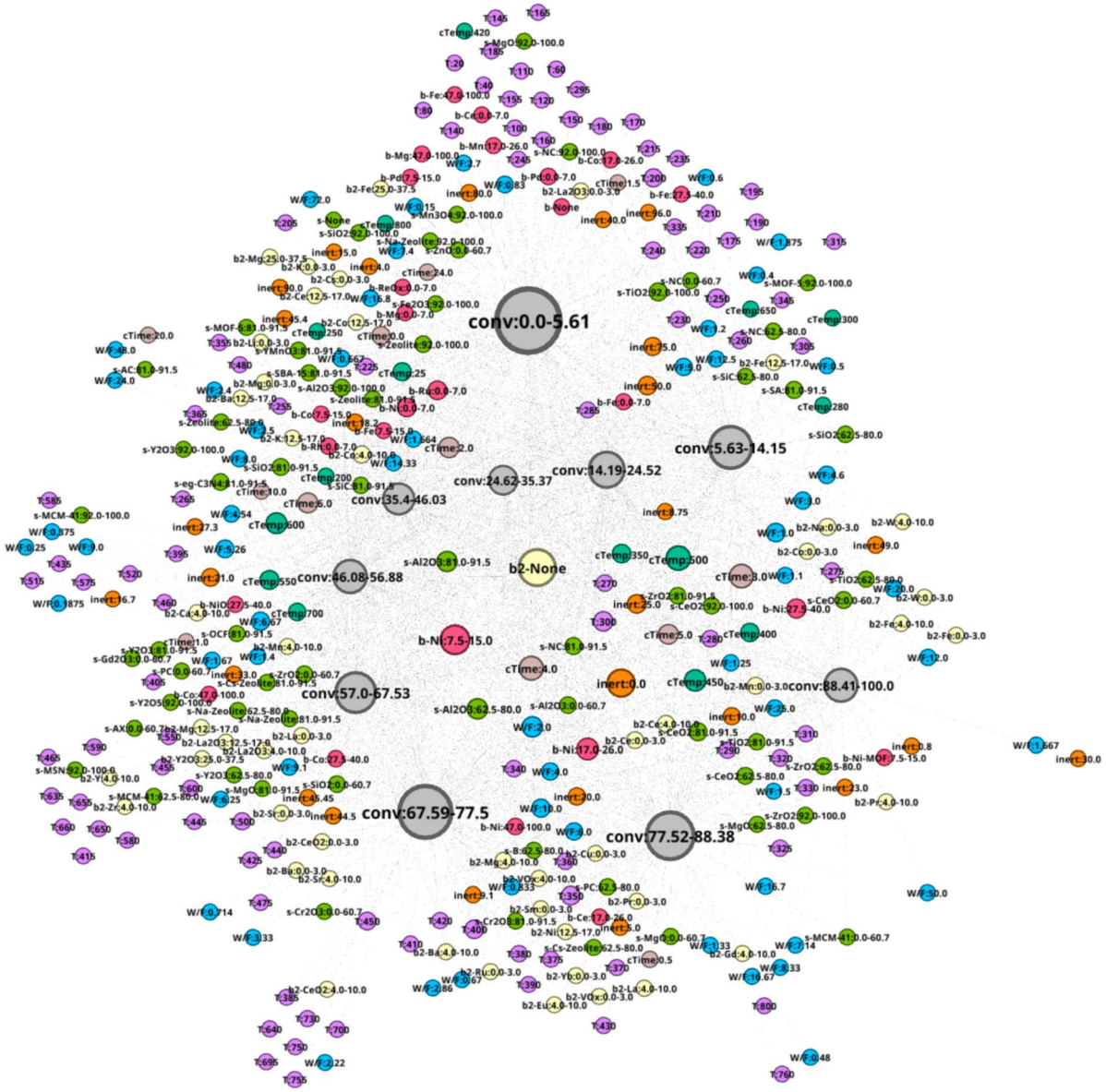

Fig. 1 The N-1 network. Each variable is color-coded: pink (base), yellow (base 2), green (support), emerald (calcination temperature (°C)), light brown (calcination time (h)), light purple (temperature (°C)), light blue (W/F (mg_{cat} min^{-1} mL^{-1})), orange (inert% in feed), and gray (CO_2 conversion, %). Note that labels are adjusted and node size is determined by degree ranking within a range of 10 to 40 for visualization purposes. A higher resolution of this network can be found in the SI.

Open Access Article. Published on 09 April 2026. Downloaded on 4/30/2026 7:20:59 AM. This article is licensed under a Creative Commons Attribution-NonCommercial 3.0 Unported Licence.

2.3.2 Catalyst activity and characterization. Catalyst performance is tested in fixed-bed quartz reactor ($L = 375$ mm, ID = 7.5 mm) under ambient pressure. The catalyst powder (100 mg) is placed between two layers of quartz wool. The reactor temperature is monitored using a K-type thermocouple, with the tip placed near the outer reactor wall of the catalyst bed location. Prior to measurement run, the system is purged at 50 °C for 20–30 min under N_2 gas at a flow of 50 mL min^{-1}, then cooled down under a $N_2/H_2/CO_2$ flow of 25/20/5 mL min^{-1}. After measuring at room temperature and confirming the absence of impurities in the outlet flow, catalyst performance is studied at 150–450 °C at 50 °C intervals under the same gas flow conditions. The reaction mixture is analyzed by using a Shimadzu GC-2014 chromatograph equipped with a SHINCARBON ST 50/80 mesh column (3 mm × 2 m, He carrier). CO_2 conversion and yield (CO and CH_4) are estimated using N_2 as an internal standard. CO_2 conversion is calculated in accordance to eqn (1) product P yield for CO and CH_4 is calculated in accordance to eqn (2), where $n = 1$ for CO and CH_4. To ensure reproducibility, each catalyst is tested twice. The 12 hours durability testing is conducted on $NiMnPr/Al_2O_3$ under H_2/CO_2 of 4 at 450 °C.

$$CO_{2Conv} = \frac{(CO_{2In}/N_{2In}) - (CO_{2Out}/N_{2Out})}{(CO_{2In}/N_{2In})} \times 100 \quad (1)$$

$$P_{Yield} = \frac{n(P_{Out}/N_{2Out})}{(CO_{2In}/N_{2In})} \times 100 \quad (2)$$

$$P_{selectivity} = \frac{P_{yield}}{CO_{2Conv}} \times 100 \quad (3)$$

Scanning electron microscopy(JEOL Neo-Scope JCM-7000), and X-ray diffraction (Rigaku MiniFlex600-C) are used in order to obtain surface condition of samples and crystal structure. XRD is performed to obtain diffraction pattern over the 2θ of 3–90 with a step size 0.01° and a scan of 10° per min.

CO_2 uptake is performed to evaluate the CO_2 adsorption–desorption properties. After degassing the samples at 300 °C for 2 h under vacuum to remove adsorbed moisture and surface impurities, CO_2 adsorption–desorption measurements are carried out using a BELSORP MINI X. CO_2 adsorption isotherms are obtained at room temperature (25 °C) by increasing the pressure from 0 to 100 kPa, and desorption are subsequently recorded by decreasing the pressure.

TPR profile is monitored with a TCD detector by BELCAT II system (MicrotracBEL, Co., Osaka, Japan). 50 mg of sample is pretreated under an He flow (30.0 mL min^{-1}) at 500 °C for 1 h, and cooled to 45 °C. H_2-TPR profile is observed under a 10 vol% H_2/Ar flow (30.0 mL min^{-1}) from 50 °C to 900 °C at the ramping rate of 10.0 °C min^{-1}. A molecular sieves 4A trap is placed at the line between an out-let of the sample bed and a TCD detector.

3 Result and discussion

3.1 Network construction and analysis

The network N-1 is constructed and analyzed to investigate the relationship between CO_2 conversion and other features as shown in Fig. 1. Construction of the N-1 network results in an undirected network which has 360 nodes and 28 248 edges. The edge weight is set to 1. Node size is determined by degree ranking within a range of 10 to 40. Node placement is determined by the relationship of a node against all other nodes within the network. As seen in Fig. 2, the network structure reveals that nodes for CO_2 conversion are placed in groups that can be interpreted as areas of low, medium, and high CO_2 conversion. The nodes for CO_2 conversion are defined as follows: low conversion: 0.00–5.61% and 5.63–14.15%; medium conversion: 35.40–46.03%, 46.08–56.88%, and 57.00–67.53%, as

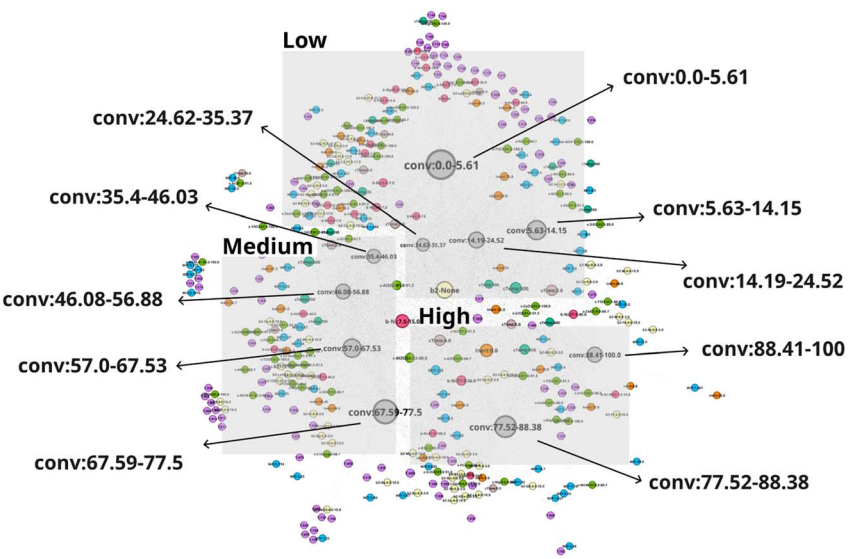

Fig. 2 A large picture of N-1. Each variable is color-coded: pink (base), yellow (base 2), green (support), emerald (calcination temperature (°C)), light brown (calcination time (h)), light purple (temperature (°C)), light blue (W/F (mg_{cat} min^{-1} mL^{-1})), orange (inert% in feed), and gray (CO_2 conversion, %). Areas up to 35.37% is defined as low CO_2 conversion area, 35.4% to 77.5% is defined as medium CO_2 conversion area, and greater than 77.52% is defined as high CO_2 conversion area. A higher resolution of this network can be found in the SI.

© 2026 The Author(s). Published by the Royal Society of Chemistry

Open Access Article. Published on 09 April 2026. Downloaded on 4/30/2026 7:20:59 AM.
This article is licensed under a Creative Commons Attribution-NonCommercial 3.0 Unported Licence.

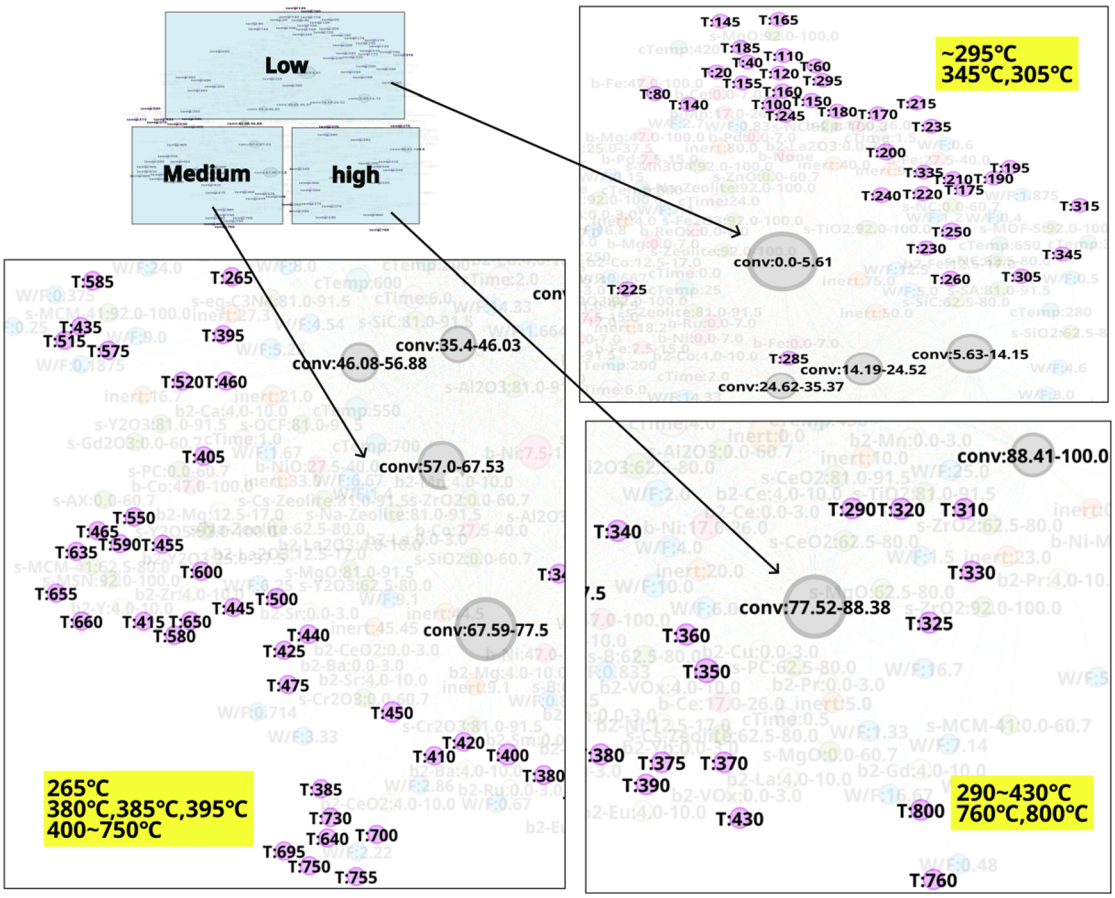

Fig. 3 Relationship between temperature (°C) and CO_2 conversion (%) based on the N-1 network which shows enlarged views of regions where temperatures are concentrated. Nodes of temperature (light purple) and CO_2 conversion (gray) are highlighted. Areas up to 35.37% is defined as low CO_2 conversion area, 35.4% to 77.5% is defined as medium CO_2 conversion area, and greater than 77.52% is defined as high CO_2 conversion area. Note that labels are adjusted, and node size is determined by degree ranking within a range of 10 to 40 for visualization purposes. A higher resolution of this network can be found in the SI.

well as 67.59–77.5%; high conversion: 77.52–88.38% and 88.41–100%. By looking at nodes found within each CO_2 conversion area, it becomes possible to understand the factors associated with that range of CO_2 conversion, thereby making it possible to include multidimensionality during analysis.

N-1 is analyzed to investigate the relationship between experiment conditions and CO_2 conversion. Temperature is found to exhibit a pronounced trend with CO_2 conversion as shown in Fig. 3. Low temperature range below 200 °C strongly correlates to low CO_2 conversion area. On the other hand, 300–400 °C temperature range is dispersed among low, medium, and high CO_2 conversion area. This suggests that CO_2 conversion may vary significantly depending on the catalyst composition and other experimental conditions within a temperature range of 300–400 °C; in this situation, temperature may have less impact on CO_2 conversion in comparison to other experimental factors. Temperature range of 400–750 °C mainly correlates to medium CO_2 conversion range, whereas 430 °C, 800 °C, and 760 °C is included to the high CO_2 conversion area. The relationship between other variables and CO_2 conversion is shown in Fig. 4. It can be seen that calcination temperatures (cTemp) of 400 or 450 °C and calcination times (cTime) of 0.5, 4.0, or 5.0 h are associated with high CO_2 conversion, whereas low or high calcination conditions (*e.g.* 25 °C, 650 °C, or 800 °C and 0 or 24 hours) are included in the area of low CO_2 conversion area. Therefore, intermediate calcination temperatures and times such as 400–450 °C and 4–5 hours, rather than low or high calcination temperatures and time, are possibly ideal conditions to consider for catalyst synthesis. As shown in Fig. 4, nodes with a high inert% in feed(inert) are associated with low CO_2 conversion, thereby showing these conditions are likely to be undesirable for achieving efficient CO_2 conversion. In this way, by converting literature data into a network and focusing on experimental conditions, it becomes possible to identify conditions that are effective for CO_2 conversion as well as those that should be avoided.

The high CO_2 conversion area in the N-1 network is focused to investigate the relationship between catalysts and CO_2 conversion. As shown in Fig. 5, Ni, Ce, and Ni–MOF used as "base 1" exhibit high CO_2 conversion. Na, Co, W, Fe, Mn, Pr, Ce, VO_x, Cu, Sm, Ni, Yb, La, Eu, Gd, and Ru are also included as "base 2." Supports include TiO_2, ZrO_2, CeO_2, MgO, MCM-41, B,

Open Access Article. Published on 09 April 2026. Downloaded on 4/30/2026 7:20:59 AM.
This article is licensed under a Creative Commons Attribution-NonCommercial 3.0 Unported Licence.

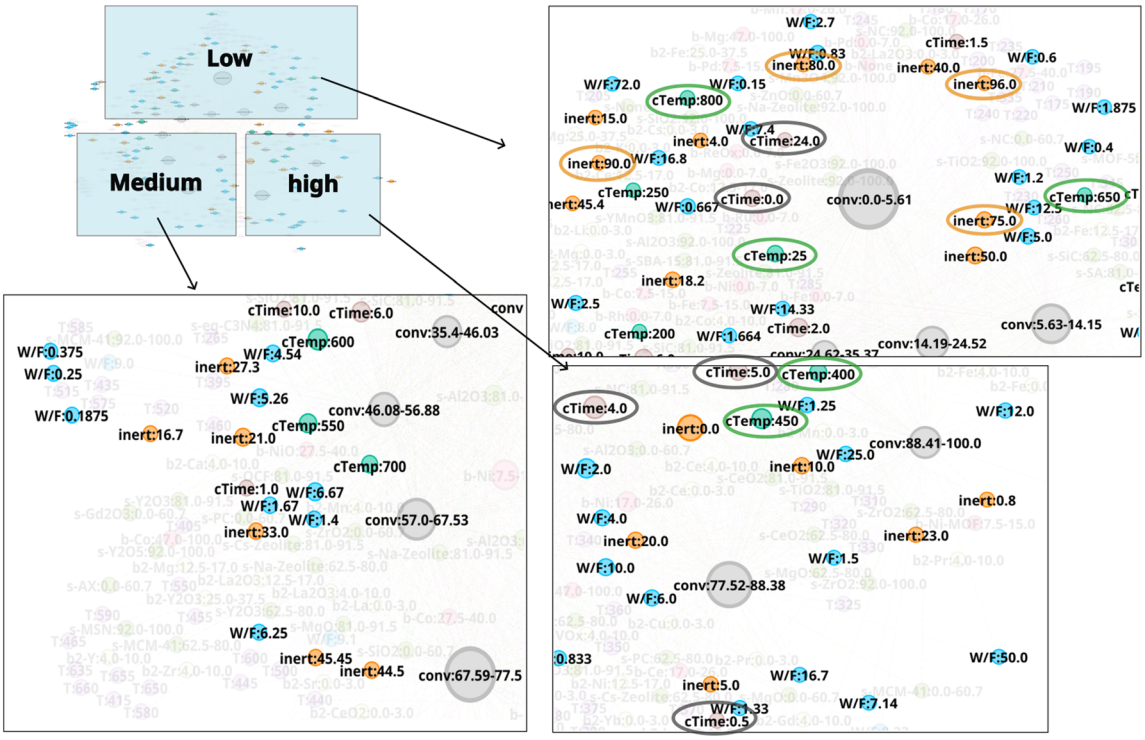

Fig. 4 Relationship between CO_2 conversion (%) and experimental conditions (W/F, inert% in feed, inert; calcination temperature (°C), cTemp; calcination time (h), cTime) based on the N-1 network. Areas up to 35.37% is defined as low CO_2 conversion area, 35.4% to 77.5% is defined as medium CO_2 conversion area, and greater than 77.52% is defined as high CO_2 conversion area. Note that labels are adjusted, and node size is determined by degree ranking within a range of 10 to 40 for visualization purposes. A higher resolution of this network can be found in the SI.

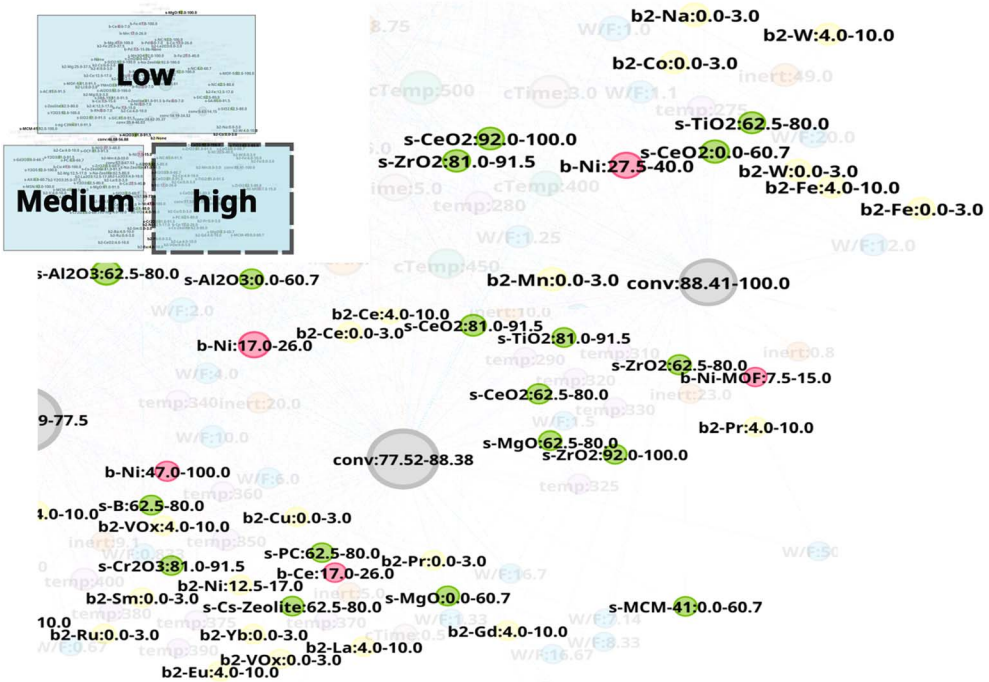

Fig. 5 Relationship between CO_2 conversion (%) and catalyst elements (base 1, b1, base 2, b2; support, s) based on the N-1 network. High CO_2 conversion area is enlarged. Areas up to 35.37% is defined as low CO_2 conversion area, 35.4% to 77.5% is defined as medium CO_2 conversion area, and greater than 77.52% is defined as high CO_2 conversion area. Note that labels are adjusted and node size is determined by degree ranking within a range of 10 to 40 for visualization purposes. A higher resolution of this network can be found in the SI.

© 2026 The Author(s). Published by the Royal Society of Chemistry

Open Access Article. Published on 09 April 2026. Downloaded on 4/30/2026 7:20:59 AM. This article is licensed under a Creative Commons Attribution-NonCommercial 3.0 Unported Licence.

Cr_2O_3, PC (porous carbon), Al_2O_3, and Cs–zeolite. Although these elements and supports are correlated with high CO_2 conversion, it is necessary to investigate the relationship between CO_2 conversion and catalyst combinations of base 1 and base 2 for a better understanding.

3.2 Catalyst screening

Another network, N-2, is constructed to explore catalyst combinations and screen for promising combinations. The N-2 network is constructed to investigate the relationship between catalyst combinations and CO_2 conversion as shown in Fig. 6. As shown in Fig. S2, base 1 and base 2 are represented as single nodes, and the relationship between element pairs and CO_2 conversion clarifies whether those pairs are effective in improving CO_2 conversion. It results in an undirected network which has 379 nodes and 24 717 edges. The edge weight is set to 1. Node size is determined by degree ranking within a range of 10 to 40. Similarly to the case of the N-1 network, the network structure reveals that nodes for CO_2 conversion are placed in groups that can be interpreted as areas of low, medium, and high CO_2 conversion as shown in Fig. 7. The nodes for CO_2 conversion are defined as follows: low conversion: 0.00–5.61% and 5.63–14.15%; medium conversion: 35.40–46.03%, 46.08–56.88%, and 57.00–67.53%, as well as 67.59–77.50%; and high conversion: 77.52–88.38% and 88.41–100%. By looking at nodes included in each CO_2 conversion area, it becomes possible to understand chemical element combinations associated with that particular range of CO_2 conversion. This, therefore, makes it possible to include compatibility of each combination during analysis.

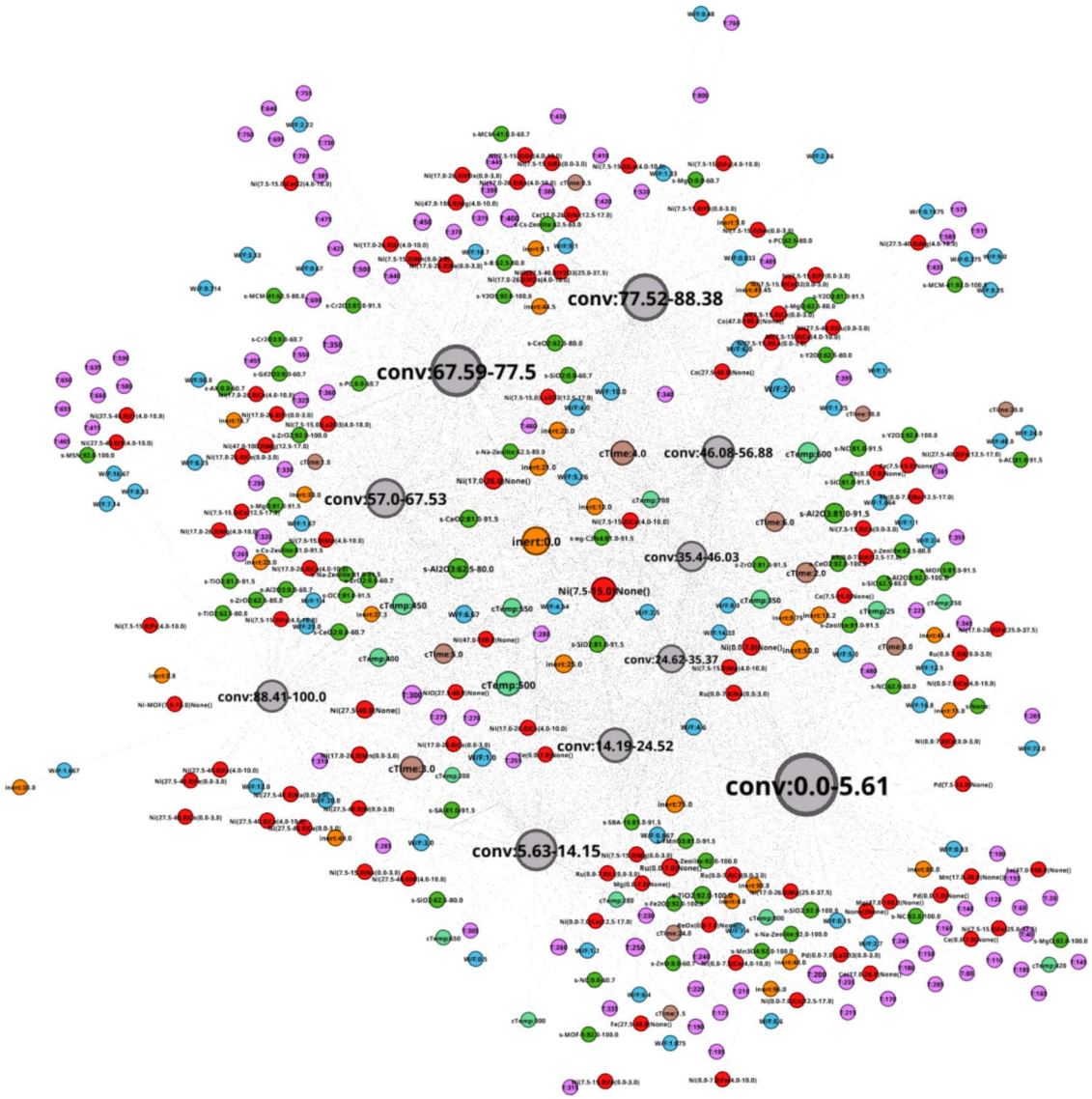

Fig. 6 The N-2 network. Each variables is color-coded: red (catalyst), green (support), emerald (calcination temperature (°C)), light brown (calcination time (h)), light purple (temperature (°C)), light blue (W/F (mg_{cat} min^{-1} mL^{-1})), orange (inert% in feed), and gray (CO_2 conversion, %). Note that labels are adjusted and node size is determined by degree ranking within a range of 10 to 40 for visualization purposes. A higher resolution of this network can be found in the SI.

Open Access Article. Published on 09 April 2026. Downloaded on 4/30/2026 7:20:59 AM.
This article is licensed under a Creative Commons Attribution-NonCommercial 3.0 Unported Licence.

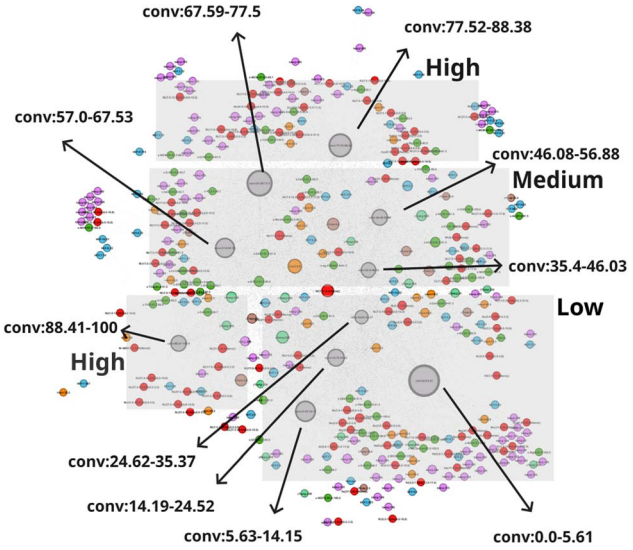

Fig. 7 A large picture of N-2. Each variables is color-coded: red (catalyst), green (support), emerald (calcination temperature (°C)), light brown (calcination time (h)), light purple (temperature (°C)), light blue (W/F (mg_{cat} min^{-1} mL^{-1})), orange (inert% in feed), and gray (CO_2 conversion, %). Areas up to 35.37% is defined as low CO_2 conversion area, 35.4% to 77.5% is defined as medium CO_2 conversion area, and greater than 77.52% is defined as high CO_2 conversion area. A higher resolution of this network can be found in the SI.

The high CO_2 conversion area in the N-2 network is investigated further to better understand the relationship between catalyst combinations and CO_2 conversion as shown in Fig. 8. It can be seen that metal combinations such as NiNa, NiCo, NiFe, NiMn, NiPr, NiCe, $NiVO_x$, NiSm, NiBa, and NiSr are associated with high CO_2 conversion area and are located near nodes of high CO_2 conversion. Elements such as Ni, Na, Co, Fe, Sm, Mn, Ce, Pr, and VO_x are also included in Fig. 5, while elements such as Ba and Sr seem to correlate with high CO_2 conversion rates when combined with Ni. In particular, the introduction of manganese into nickel-based catalysts has been demonstrated to enhance CO_2 conversion.[33–37] Furthermore, other combinations such as NiCe, NiPr, NiBa, NiFe, and NiCo, which are screened from Fig. 8, have also been reported to improve CO_2 conversion.[38–42] Therefore, such catalytic networks appropriately represent the trends observed in literature data across different CO_2 conversion areas. Catalyst combinations associated with low CO_2 conversion are also examined as shown in Fig. S3. In this area, combinations such as NiCo, NiCe, NiMg, and NiFe are observed. Notably, Co, Ce, and Fe also appear in the high CO_2 conversion area, suggesting that the apparent overlap is largely governed by the elemental composition rather than by the presence of a given element alone. As shown in Fig. 8, the promoter contents in the high CO_2 conversion area remain limited to a few percent relative to Ni such as Ni(27.5–40.0)Co(0.0–3.0), Ni(27.5–40.0)Ce(4.0–10.0), and Ni(27.5–40.0)Fe(4.0–10.0). In contrast, Fig. S3 indicates that low CO_2 conversion catalysts often involve comparatively excessive promoter loadings relative to Ni such as Ni(0.0–7.0)Co(12.5–17.0), Ni(0.0–7.0)Ce(12.5–17.0), and Ni(7.5–15.0)Fe(25.0–37.5). It should be noted, however, that the low CO_2 conversion area also includes compositions with low promoter contents such as Ni(7.5–15.0)Fe(0.0–3.0) and Ni(17.0–26.0)Co(4.0–10.0). Taken together, these observations indicate that excessive promoter addition is an unfavorable condition for achieving high CO_2

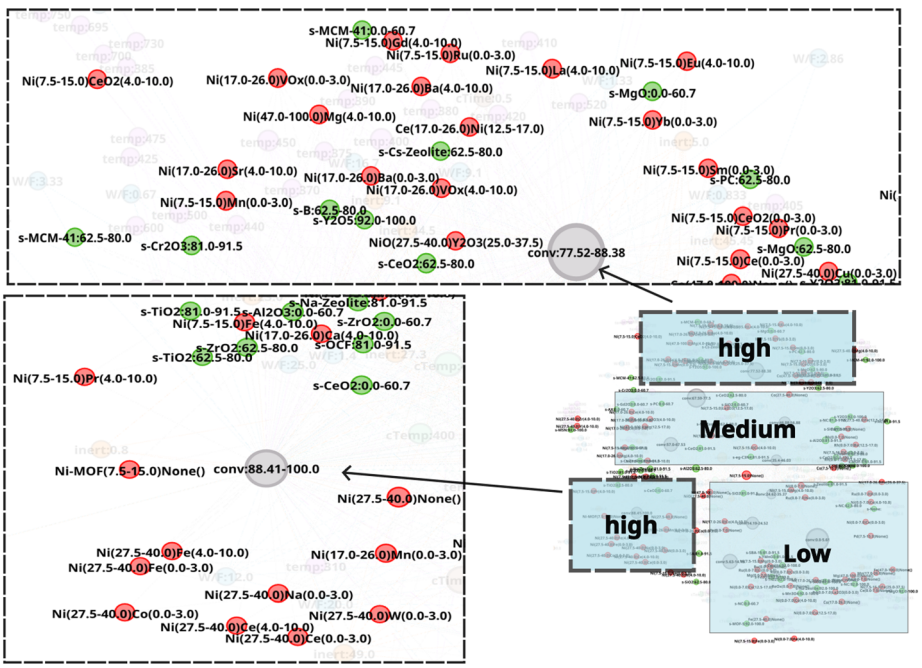

Fig. 8 Details of high CO_2 conversion area in the N-2 network. Catalyst (pink), support (green), and CO_2 conversion (gray) are highlighted. Note that labels are adjusted and node size is determined by degree ranking within a range of 10 to 40 for visualization purposes. A higher resolution of this network can be found in the SI.

© 2026 The Author(s). Published by the Royal Society of Chemistry

Open Access Article. Published on 09 April 2026. Downloaded on 4/30/2026 7:20:59 AM.
This article is licensed under a Creative Commons Attribution-NonCommercial 3.0 Unported Licence.

conversion. The network analysis reveals that certain metal combinations and compositions are systematically associated with CO_2 conversion. Therefore, employing these combinations and compositions may contribute to improving CO_2 conversion based off the trends and information present in these networks. In this study, a systematic screening of metal combinations to identify promising ternary catalysts is performed. To evaluate whether the knowledge extracted from the binary catalysts data can be extended to the design of ternary catalysts, a representative subset of screened ternary candidates (NiMnPr, NiMnCe, NiMnBa, NiMnFe, and NiMnCo) are selected. Al_2O_3 is selected as the standard support in all catalysts for comparing the activity of element pairs.

3.3 Catalyst performance

To evaluate the activity of the screened catalysts, the performance of ternary catalysts is tested at a temperature range of 150–450 °C. For comparison, CO_2 conversion of $NiMn/Al_2O_3$, $NiCe/Al_2O_3$, $NiPr/Al_2O_3$, and Ni/Al_2O_3 catalysts are also examined. All three element catalysts exhibit better activity compared to Ni/Al_2O_3. Furthermore the effectiveness of three element catalysts become more pronounced when compared to $NiMn/Al_2O_3$. At 400 °C, the CO_2 conversion follows the order: $NiMnCe/Al_2O_3$ (58.02%) > $NiMnPr/Al_2O_3$ (57.33%) > $NiMnBa/Al_2O_3$ (49.61%) > $NiMn/Al_2O_3$ (48.65%) > $NiMnCo/Al_2O_3$ (36.70%) > $NiMnNa/Al_2O_3$ (31.68%) > $NiMnFe/Al_2O_3$ (27.99%). The CH_4 yield follows the order: $NiMnPr/Al_2O_3$ (40.53%) > $NiMnCe/Al_2O_3$ (39.24%) > $NiMn/Al_2O_3$ (30.21%) ≃ $NiMnBa/Al_2O_3$ (30.07%) > $NiMnCo/Al_2O_3$ (16.66%) > $NiMnFeAl/_2O_3$ (8.99%) > $NiMnNa/Al_2O_3$ (6.67%). Interestingly, $NiMnCe/Al_2O_3$ and $NiMnPr/Al_2O_3$ exhibit higher CO_2 conversion than $NiCe/Al_2O_3$ (39.22%) and $NiPr/Al_2O_3$ (10.86%), possibly due to additional effects among the three elements, as shown in Fig. 9(a). Furthermore, a 12 h durability testing is conducted on $NiMnPr/Al_2O_3$, which exhibits the highest CH_4 yield, and it demonstrated excellent stability as

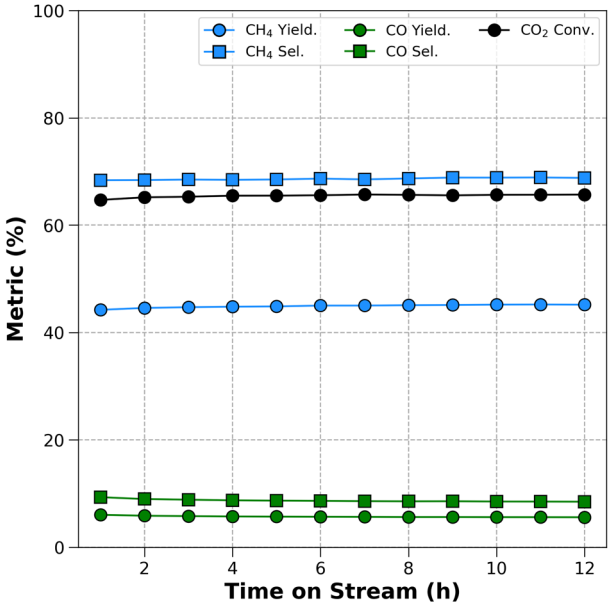

Fig. 10 A 12 h durability test for $NiMnPr/Al_2O_3$ at 450° under H_2/CO_2 of 4.

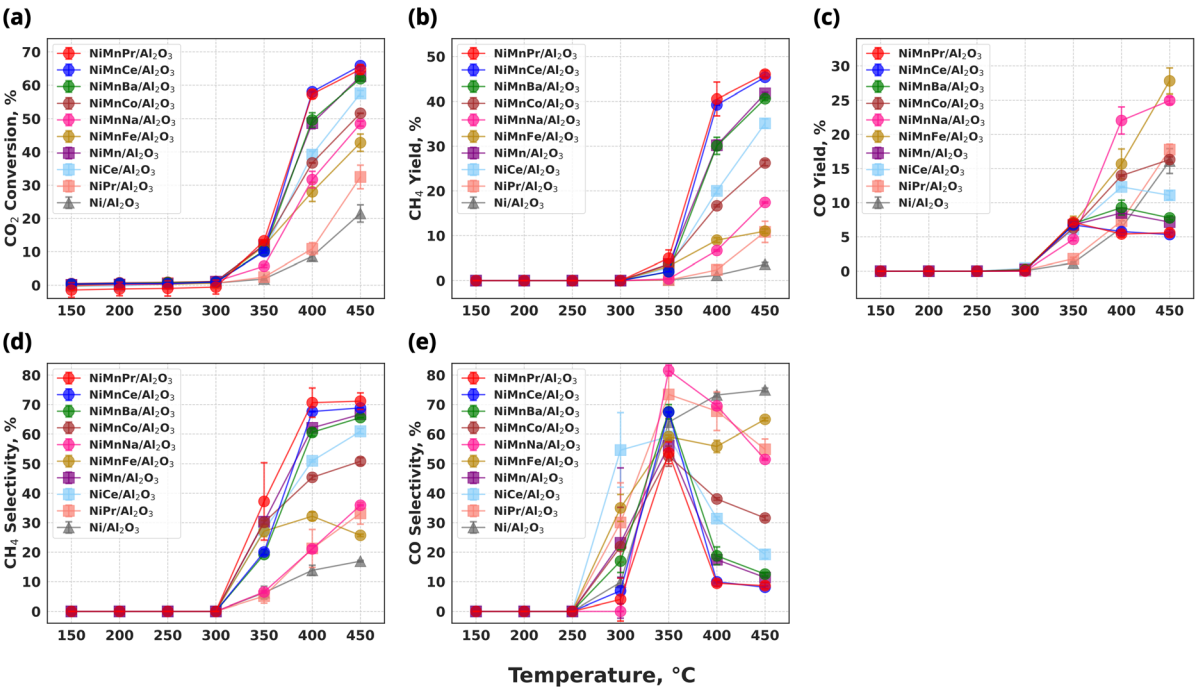

Fig. 9 (a) CO_2 conversion, %, (b) CH_4 yield, %, (c) CO yield, %, (d) CH_4 selectivity, %, and (e) CO selectivity, % as a function of temperature. Ternary, binary, and unary catalysts are represented by circles, squares, and triangles, respectively. Note that the plots and error bars at each temperature represent the average and standard deviation of two measurements to ensure reproducibility.

Open Access Article. Published on 09 April 2026. Downloaded on 4/30/2026 7:20:59 AM. This article is licensed under a Creative Commons Attribution-NonCommercial 3.0 Unported Licence.

shown in Fig. 10. More detailed results for catalysts containing Ni, Mn, and/or Pr are shown in Fig. S4, and a comparison with previously reported catalysts is shown in Table S1. CO_2 conversion and CH_4 yield of $NiMnBa/Al_2O_3$ are comparable to those of $NiMn/Al_2O_3$, whereas $NiMnCo/Al_2O_3$, $NiMnNa/Al_2O_3$, and $NiMnFe/Al_2O_3$ reduce CO_2 conversion and suppress methane formation as shown in Fig. 9(a), (b) and (d). Furthermore, as shown in Fig. 9(c) and (e), $NiMnCe/Al_2O_3$, $NiMnPr/Al_2O_3$, and $NiMnBa/Al_2O_3$ can suppress CO formation, whereas $NiMnCo/Al_2O_3$, $NiMnFe/Al_2O_3$, and $NiMnNa/Al_2O_3$ exhibit increased CO yield with rising temperature. Consequently, the activity for CO_2 hydrogenation changes significantly depending on the element added to NiMn. In other words, pairing Ni–Mn with a lanthanoid element resulted in higher yields compared to transition (Fe, Co) and basic metals (Na, Ba). In particular, $NiMnCe/Al_2O_3$ and $NiMnPr/Al_2O_3$ exhibit higher CO_2 conversion than corresponding binary catalysts, demonstrating their potential as promising catalysts.

3.4 Characterization on $NiMnPr/Al_2O_3$

The $NiMnPr/Al_2O_3$ catalyst, which exhibits the highest CH_4 yield, is selected for detailed characterization to identify the physicochemical features responsible for its superior performance. XRD is investigated to confirm the crystal structure. The XRD patterns of catalysts containing Ni, Mn, and/or Pr are shown in Fig. 11(a), while those of the other catalysts are provided in Fig. S5. As shown in Fig. 11(a), XRD patterns show the characteristic diffraction peaks of γ-alumina, whereas no peaks corresponding to the Ni, Mn, and Pr are detected. The absence of peaks indicates that either the concentration of the crystalline phase of the species containing the impregnated elements is very low or they are not forming crystalline phases. Furthermore, no differences in peak intensity or shift are observed among catalysts.

SEM-EDS analyses is conducted to confirm morphology and surface compositions of the synthesized catalysts. As shown in Fig. 11(b), although no peaks related to Mn, Ni, or Pr are

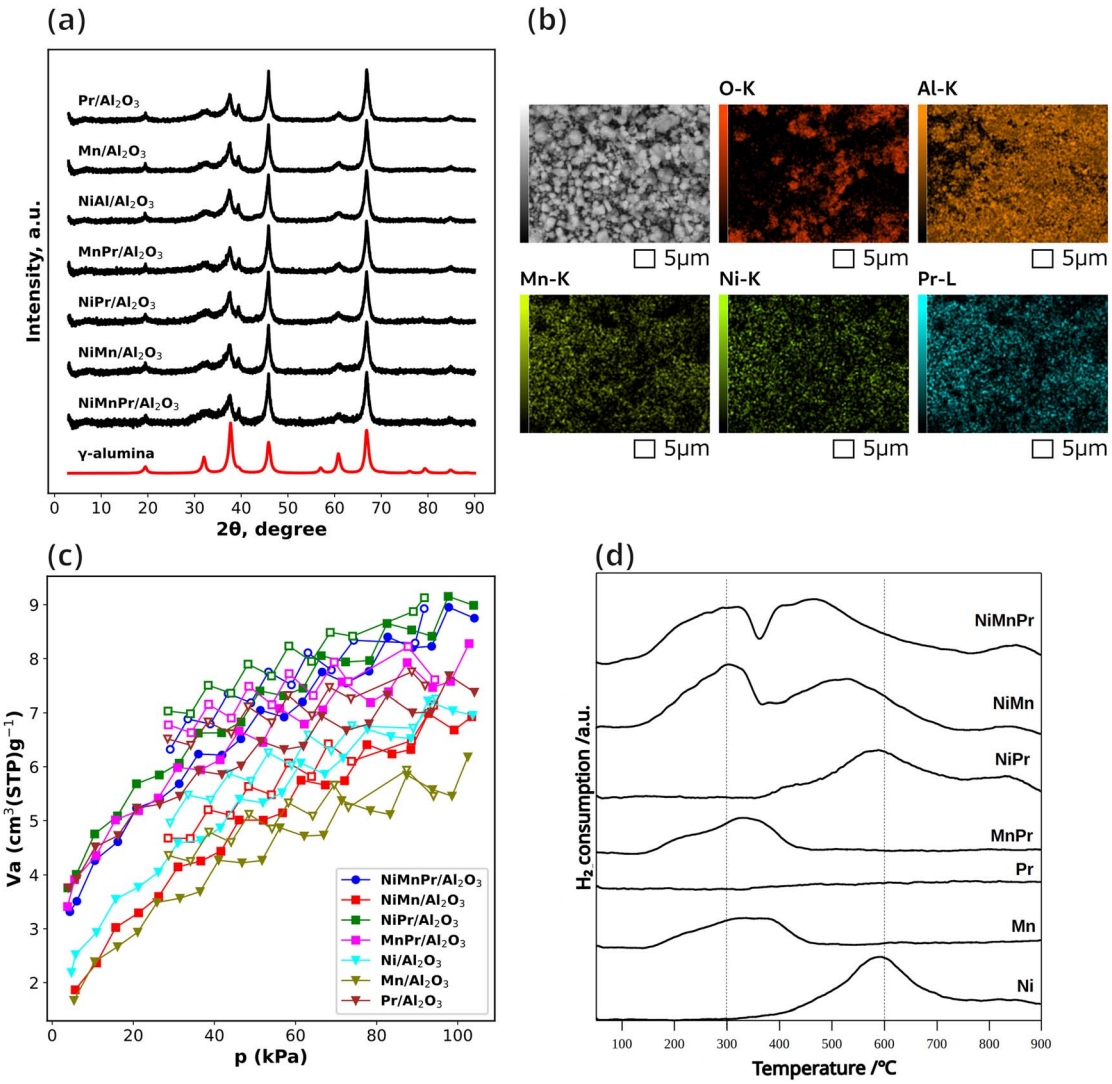

Fig. 11 (a) XRD for catalysts with Ni, Pr, or Mn. The reference pattern shown in red is obtained from the built-in database of the Rigaku Miniflex 600-C software. (b) The SEM-EDS image for $NiMnPr/Al_2O_3$. (c) CO_2 adsorption and desorption for catalysts with Ni, Pr, or Mn. (d) H_2-TPR profiling for catalysts with Ni, Pr, or Mn.

© 2026 The Author(s). Published by the Royal Society of Chemistry

Open Access Article. Published on 09 April 2026. Downloaded on 4/30/2026 7:20:59 AM. This article is licensed under a Creative Commons Attribution-NonCommercial 3.0 Unported Licence.

observed in XRD, SEM-EDS confirms the presence of these three elements. The catalyst appears as an agglomeration with an average diameter of approximately 5 μm. SEM-EDS elemental mapping confirms the presence of Ni, Mn, and Pr on the γ-Al_2O_3 support. The Ni–K, Mn–K, and Pr–L maps show broadly distributed signals over the observed area indicating good dispersion at the micrometer scale. SEM-EDS for other catalysts also shows in Fig. S6–S8.

CO_2 adsorption–desorption measurements are performed to investigate the CO_2 related properties of the catalysts. As shown in Fig. 11(c), the CO_2 uptake is in the order of Pr/Al_2O_3, $NiAl_2O_3$, $MnAl_2O_3$ for the unary catalysts. $NiPr/Al_2O_3$ exhibits the highest CO_2 uptake, followed by $NiMnPr/Al_2O_3$ with a nearly comparable value, and then by $MnPr/Al_2O_3$ and Pr/Al_2O_3, whereas other Pr-free catalysts have relatively lower CO_2 uptake. It is considered that Pr-containing catalyst systems enhance CO_2 adsorption and activation.[43] In other words, the addition of Pr to Ni or Ni–Mn catalysts increases CO_2 uptake. This result is consistent with the higher CO_2 conversion and CH_4 yield observed for the NiMnPr and NiPr catalysts compared with the NiMn and Ni catalysts at 400 °C, as shown in Fig. 9(a) and (b). Therefore, the Pr in the ternary catalyst may also contribute to changes in surface properties related to CO_2.

The results of H_2-TPR profile are shown in Fig. 11(d). Ni/Al_2O_3 indicates a large reduction peak at 600 °C from 300 °C to 800 °C, attributed to the reduction of NiO to Ni metal. Mn/Al_2O_3 gives broad peak at around 150–500 °C, derived from sequential reduction steps of Mn oxides such as MnO_2 to Mn_2O_3, Mn_3O_4 and MnO. Pr/Al_2O_3 does not serve any obvious reduction profile below 900 °C. The addition of Pr to Mn or Ni slightly increases the shoulder peak area at lower temperature, which is likely due to an increase in the number of easily reduced Mn or Ni species. There are significant differences in binary NiMn and ternary NiMnPr catalysts in comparison to unary Ni and Mn catalysts. Both NiMn and NiMnPr catalysts possess two-humped reduction peak. It is considered that the lower temperature profile at 100–350 °C from MnO_2 into Mn_2O_3 and Mn_2O_3 into MnO whereas the higher temperature profile 350–750 °C from NiO into Ni origin, respectively.[36] It is very interesting that the peak at higher temperature derived from Ni origin gives gradual shift to the lower temperature at the top peak from 585 °C ($NiAl_2O_3$), 530 °C ($NiMnAl_2O_3$) to 475 °C ($NiMnPrAl_2O_3$). The improved reducibility of NiO contributes to the fine dispersion of the as-generated Ni. As the result, higher catalytic activity is observed in the binary $NiMn/Al_2O_3$ systems in earlier studies.[44,45] This trend is consistent with the enhanced CO_2 conversion and CH_4 yield observed for these catalysts as shown in Fig. 9(a) and (b). Overall, considering CO_2 uptake and H_2-TPR profile, the unique NiMnPr catalyst, which is experimentally validated as facilitating CO_2 methanation at lower temperatures, clearly indicates the effect of additive Pr for further improvement of NiMn nature.

4 Conclusions

CO_2 hydrogenation dataset is utilized to structure multidimensional data *via* network analysis. The constructed networks provide insights into which experimental conditions are effective or not for the catalysts data across multidimensional variables. Furthermore, the networks are applied to catalyst screening, identifying useful catalyst combinations. Six ternary element catalysts selected from high CO_2 conversion area are developed and experimentally validated. $NiMnPr/Al_2O_3$ and $NiMnCe/Al_2O_3$ demonstrate activity exceeding that of their respective binary element catalysts. This result demonstrates that network-based trends and knowledge can efficiently discover new catalysts. This approach not only uncovers key trends and relationships across multidimensional variables in complex heterogeneous reactions but also establishes a generalizable strategy for guiding the design of efficient catalysts. These findings highlight the potential of data-driven network methodologies to accelerate catalyst discovery and provide a framework for exploring complex catalytic systems.

Author contributions

Y. H.: Conceptualization, network construction and analysis, experimental investigation and analysis. F. G.-E.: Experimental investigation and analysis, validation. S. N.: Experimental investigation and analysis. K. T.: Supervision, validation, funding. L. T.: Supervision, network analysis, validation, funding. All authors were involved in reviewing and editing the manuscript.

Conflicts of interest

There are no conflicts to declare.

Data availability

All data is provided in the manuscript.

Supplementary information (SI): source dataset (xlsx), support information (pdf), high-resolution Fig. 1 (png), and high-resolution Fig. 6 (png). Raw chromatograms and calculated catalyst activities from activity test. See DOI: https://doi.org/10.1039/d6sc00563b.

Acknowledgements

This work is funded by the Japan Science and Technology Agency (JST) ERATO grant number (JPMJER1903), PRESTO grant number (JPMJPR24T5), and JST Mirai Program grant number (JP-MJMI25G1), JSPS KAKENHI Grant-in-Aid for Scientific Research (B) grant number (JP23H01762) and (24K01241). This work is also supported by the research fund "Hokkaido University-Hitachi Joint Cooperative Support Program for Education and Research".

References

1 C. Junaedi, K. Hawley, D. Walsh, S. Roychoudhury, M. Abney and J. Perry, Compact and lightweight Sabatier reactor for carbon dioxide reduction, in *41st International Conference on Environmental Systems*, 2011, p. 5033.

Open Access Article. Published on 09 April 2026. Downloaded on 4/30/2026 7:20:59 AM. This article is licensed under a Creative Commons Attribution-NonCommercial 3.0 Unported Licence.

2 S. Romegialli, A. Tripodi, A. Gramegna, M. Tommasi, G. Ramis and I. Rossetti, Production of Synthetic Methane for Aerospace Applications: A Mars Case, *Ind. Eng. Chem. Res.*, 2024, **64**, 190–208.
3 K. Ghaib, K. Nitz and F.-Z. Ben-Fares, Chemical methanation of CO_2: a review, *ChemBioEng Rev.*, 2016, **3**, 266–275.
4 M. Tommasi, S. N. Degerli, G. Ramis and I. Rossetti, Advancements in CO_2 methanation: a comprehensive review of catalysis, reactor design and process optimization, *Chem. Eng. Res. Des.*, 2024, **201**, 457–482.
5 G. Liu, S. Sun, H. Sun, Y. Zhang, J. Lv, Y. Wang, J. Zeng, Z. Yan and C. Wu, Integrated CO_2 capture and utilisation: a promising step contributing to carbon neutrality, *Carbon Capture Sci. Technol.*, 2023, **7**, 100116.
6 W. J. Lee, C. Li, H. Prajitno, J. Yoo, J. Patel, Y. Yang and S. Lim, Recent trend in thermal catalytic low temperature CO_2 methanation: a critical review, *Catal. Today*, 2021, **368**, 2–19.
7 W. K. Fan and M. Tahir, Recent trends in developments of active metals and heterogenous materials for catalytic CO_2 hydrogenation to renewable methane: a review, *J. Environ. Chem. Eng.*, 2021, **9**, 105460.
8 N. Rui, X. Zhang, F. Zhang, Z. Liu, X. Cao, Z. Xie, R. Zou, S. D. Senanayake, Y. Yang, J. A. Rodriguez, *et al.*, Highly active Ni/CeO_2 catalyst for CO_2 methanation: preparation and characterization, *Appl. Catal. B Environ.*, 2021, **282**, 119581.
9 H. Sun, J. Lv, C. Wang, Y. Zhang, S. Sun, P. Zhang, G. Cheng, D. Mei, Y. Wang and Z. Yan, Ru/CeO_2 catalysts with enriched oxygen vacancies by plasma treatment for efficient CO_2 methanation, *Fuel*, 2025, **381**, 133413.
10 S. Kuhaudomlap, A. Srifa, W. Koo-Amornpattana, C. Fukuhara and S. Ratchahat, Insight and comprehensive study of Ni-based catalysts supported on various metal oxides for CO_2 methanation, *Sci. Rep.*, 2024, **14**, 23149.
11 L. Shen, J. Xu, M. Zhu and Y. Han, Essential role of the support for nickel-based CO_2 methanation catalysts, *ACS Catal.*, 2020, **10**, 14581–14591.
12 S. Tada, T. Jinushizono, K. Ishikawa, S. Miyazaki, T. Toyao, K.-i. Shimizu, M. Nishijima, N. Yamauchi, Y. Kobayashi and R. Kikuchi, Low-temperature CO_2 methanation over Ru nanoparticles supported on monoclinic zirconia, *Energy Fuels*, 2024, **38**, 2296–2304.
13 A. Quindimil, U. De-La-Torre, B. Pereda-Ayo, A. Davó-Quiñonero, E. Bailón-García, D. Lozano-Castello, J. A. González-Marcos, A. Bueno-López and J. R. González-Velasco, Effect of metal loading on the CO_2 methanation: a comparison between alumina supported Ni and Ru catalysts, *Catal. Today*, 2020, **356**, 419–432.
14 M. Younas, L. Loong Kong, M. J. Bashir, H. Nadeem, A. Shehzad and S. Sethupathi, Recent advancements, fundamental challenges, and opportunities in catalytic methanation of CO_2, *Energy Fuels*, 2016, **30**, 8815–8831.
15 O. E. Medina, A. A. Amell, D. López and A. Santamaría, Comprehensive review of nickel-based catalysts advancements for CO_2 methanation, *Renew. Sustain. Energy Rev.*, 2025, **207**, 114926.
16 C. Molinet-Chinaglia, S. Shafiq and P. Serp, Low temperature Sabatier CO_2 methanation, *ChemCatChem*, 2024, **16**, e202401213.
17 F. Ahmad, E. C. Lovell, H. Masood, P. J. Cullen, K. K. Ostrikov, J. A. Scott and R. Amal, Low-temperature CO_2 methanation: synergistic effects in plasma-Ni hybrid catalytic system, *ACS Sustain. Chem. Eng.*, 2020, **8**, 1888–1898.
18 C. Wei, H. Ding, Z. Zhang, F. Lin, Y. Xu and W. Pan, Research progress of bimetallic catalysts for CO_2 hydrogenation to methane, *Int. J. Hydrogen Energy*, 2024, **58**, 872–891.
19 J. Shi, On the synergetic catalytic effect in heterogeneous nanocomposite catalysts, *Chem. Rev.*, 2013, **113**, 2139–2181.
20 A. Vojvodic and J. K. Nørskov, New design paradigm for heterogeneous catalysts, *Natl. Sci. Rev.*, 2015, **2**, 140–143.
21 T. Toyao, Z. Maeno, S. Takakusagi, T. Kamachi, I. Takigawa and K.-i. Shimizu, Machine learning for catalysis informatics: recent applications and prospects, *ACS Catal.*, 2019, **10**, 2260–2297.
22 K. Takahashi, J. Ohyama, S. Nishimura, J. Fujima, L. Takahashi, T. Uno and T. Taniike, Catalysts informatics: paradigm shift towards data-driven catalyst design, *Chem. Commun.*, 2023, **59**, 2222–2238.
23 K. Takahashi, L. Takahashi, S. D. Le, T. Kinoshita, S. Nishimura and J. Ohyama, Synthesis of heterogeneous catalysts in catalyst informatics to bridge experiment and high-throughput calculation, *J. Am. Chem. Soc.*, 2022, **144**, 15735–15744.
24 J. Benavides-Hernandez and F. Dumeignil, From characterization to discovery: artificial intelligence, machine learning and high-throughput experiments for heterogeneous catalyst design, *ACS Catal.*, 2024, **14**, 11749–11779.
25 F. Garcia-Escobar, L. Takahashi, A. Shaaban, S. Nishimura and K. Takahashi, Design of low temperature La_2O_3 oxidative coupling of methane catalysts using feature engineering and automated sampling, *Catal. Sci. Technol.*, 2025, **15**, 92–99.
26 B. Yılmaz, B. Oral and R. Yıldırım, Machine learning analysis of catalytic CO_2 methanation, *Int. J. Hydrogen Energy*, 2023, **48**, 24904–24914.
27 C. Rudin, Stop explaining black box machine learning models for high stakes decisions and use interpretable models instead, *Nat. Mach. Intell.*, 2019, **1**, 206–215.
28 Y. Hasukawa, F. Garcia-Escobar, K. Takahashi and L. Takahashi, Multidimensional Catalysis Data Representation for Designing Oxidative Coupling of Methane Catalysts, *J. Phys. Chem. C*, 2024, **129**, 391–401.
29 L. Takahashi, T. Yamada, H. Okamoto and K. Takahashi, Unveiling the relation between multiple chemical products and process conditions for trichloroethylene and perchloroethylene production via catalysis network analysis, *Catal. Sci. Technol.*, 2024, **14**, 4927–4938.
30 L. Takahashi, T. N. Nguyen, S. Nakanowatari, A. Fujiwara, T. Taniike and K. Takahashi, Constructing catalyst knowledge networks from catalyst big data in oxidative

© 2026 The Author(s). Published by the Royal Society of Chemistry

Open Access Article. Published on 09 April 2026. Downloaded on 4/30/2026 7:20:59 AM. This article is licensed under a Creative Commons Attribution-NonCommercial 3.0 Unported Licence.

coupling of methane for designing catalysts, *Chem. Sci.*, 2021, **12**, 12546–12555.

31 M. Jacomy, T. Venturini, S. Heymann and M. Bastian, ForceAtlas2, a continuous graph layout algorithm for handy network visualization designed for the Gephi software, *PLoS One*, 2014, **9**, e98679.

32 M. Bastian, S. Heymann and M. Jacomy, Gephi: an open source software for exploring and manipulating networks, in *Proceedings of the international AAAI conference on web and social media*, 2009, pp. 361–362.

33 W. L. Vrijburg, E. Moioli, W. Chen, M. Zhang, B. J. Terlingen, B. Zijlstra, I. A. Filot, A. Züttel, E. A. Pidko and E. J. Hensen, Efficient base-metal $NiMn/TiO_2$ catalyst for CO_2 methanation, *ACS Catal.*, 2019, **9**, 7823–7839.

34 D. Qiang, T. Mei, Y. Liu, Z. Ye, Z. Li and S. Zhao, High-Performance NiMn-LDO Catalysts for Efficient CO_2 Methanation, *Langmuir*, 2025, **41**, 14790–14799.

35 D. Qiang, T. Mei, Y. Liu, H. Jin, Z. Ye, Z. Li and S. Zhao, Enhanced low-temperature activity for CO_2 methanation over N-doped NiMn-LDO, *Chem. Eng. J.*, 2025, **507**, 160839.

36 W. Zhang, L. Xu, F. Zhou, F. Sun, J. Xu, M. Zhu, *et al.*, Manganese-promoted Ni/Al_2O_3 catalysts for effective CO_2 methanation, *J. Catal.*, 2025, **448**, 116215.

37 T. Burger, F. Koschany, O. Thomys, K. Köhler and O. Hinrichsen, CO_2 methanation over Fe-and Mn-promoted co-precipitated Ni-Al catalysts: synthesis, characterization and catalysis study, *Appl. Catal., A*, 2018, **558**, 44–54.

38 W. Wang, W. Chu, N. Wang, W. Yang and C. Jiang, Mesoporous nickel catalyst supported on multi-walled carbon nanotubes for carbon dioxide methanation, *Int. J. Hydrogen Energy*, 2016, **41**, 967–975.

39 W. Ahmad, M. N. Younis, R. Shawabkeh and S. Ahmed, Synthesis of lanthanide series (La, Ce, Pr, Eu & Gd) promoted $Ni/\gamma\text{-}Al_2O_3$ catalysts for methanation of CO_2 at low temperature under atmospheric pressure, *Catal. Commun.*, 2017, **100**, 121–126.

40 C. Liang, X. Hu, T. Wei, P. Jia, Z. Zhang, D. Dong, S. Zhang, Q. Liu and G. Hu, Methanation of CO_2 over Ni/Al_2O_3 modified with alkaline earth metals: impacts of oxygen vacancies on catalytic activity, *Int. J. Hydrogen Energy*, 2019, **44**, 8197–8213.

41 D. Pandey and G. Deo, Effect of support on the catalytic activity of supported Ni–Fe catalysts for the CO_2 methanation reaction, *J. Ind. Eng. Chem.*, 2016, **33**, 99–107.

42 B. Alrafei, I. Polaert, A. Ledoux and F. Azzolina-Jury, Remarkably stable and efficient Ni and Ni-Co catalysts for CO_2 methanation, *Catal. Today*, 2020, **346**, 23–33.

43 Y. Ju, D. Bae, J. Park, H. W. Choi, J. Kang, K.-H. Ryu, Y. J. Kim, M. Kim and S. B. Kang, Role of electronic modulation of Ni-Pr bimetallic catalyst for low-temperature CO_2 methanation, *Appl. Catal. B Environ. Energy*, 2025, **379**, 125675.

44 T. A. Le, J. Kim, J. K. Kang and E. D. Park, CO and CO_2 methanation over M (M = Mn, Ce, Zr, Mg, K, Zn, or V)-promoted $Ni/Al@Al_2O_3$ catalysts, *Catal. Today*, 2020, **348**, 80–88.

45 L. Huang, F. Zhang, R. Chen and A. T. Hsu, Manganese-promoted nickel/alumina catalysts for hydrogen production via auto-thermal reforming of ethanol, *Int. J. Hydrogen Energy*, 2012, **37**, 15908–15913.